

## Tailoring the Biocidal Activity of Novel Silver-Based Metal Azolate Frameworks

S. Fatemeh Seyedpour,<sup>○</sup> Ahmad Arabi Shamsabadi,<sup>○</sup> Saeed Khoshhal Salestan,<sup>○</sup> Mostafa Dadashi Firouzjaei,<sup>○</sup> Mohammad Sharifian Gh, Ahmad Rahimpour,\* Farhad Akbari Afkhami, Mohammad Reza Shirzad Kebria, Mark A. Elliott,\* Alberto Tiraferri, Marco Sangermano, Milad R. Esfahani, and Masoud Soroush\*



Cite This: *ACS Sustainable Chem. Eng.* 2020, 8, 7588–7599



Read Online

ACCESS |

Metrics & More

Article Recommendations

Supporting Information

**ABSTRACT:** The synthesis of nanostructures with tunable antibacterial properties using green solvents at room temperature is of environmental interest, and antibacterial nanomaterials are used in the fabrication of biofouling-resistant membranes for water purification and wastewater treatment. In this study, we investigate the effect of organic ligands on the antibacterial and structural properties of silver-based metal–azolate frameworks (Ag-MAFs). Three new Ag-MAFs were synthesized with silver, as the metal center, and imidazole-based linkers having different chemistries via a facile and environmentally friendly method conducted at room temperature. The coordination of silver ions with the linkers resulted in the formation of Ag-imidazole, Ag-2 methylimidazole, and Ag-benzimidazole complexes with octahedral, hexagonal nanosheet, and nanoribbon morphologies, respectively. The Ag-MAFs exhibited excellent antibacterial activity (up to 95% die-off of bacteria at a short exposure time of 3 h) in colloidal forms against both Gram-negative *Escherichia coli* (*E. coli*) and Gram-positive *Bacillus subtilis* (*B. subtilis*) because of synergistic effects of silver and the imidazole-based linkers. Ag-2 methylimidazole showed the highest antibacterial activity, owing to its high silver concentration and special nanocrystal structure that provides better contact with bacteria. This work indicates that the antibacterial activity of Ag-MAF nanostructures can be tailored by changing the organic linker, allowing for creating nanostructures with desired biocidal properties.

**KEYWORDS:** silver, metal–azolate frameworks, nanostructures, antibacterial activity



### INTRODUCTION

Pathogenic bacteria are increasingly posing a serious threat to public health because of their intrinsic antibiotic resistance.<sup>1</sup> Multidrug-resistant bacteria are forecast to cause the highest rate of death by 2050.<sup>2–4</sup> This global threat can be lessened by combatting the spread of current pathogens through the development and use of effective and nonspecific antibacterial and disinfectant materials.<sup>5,6</sup>

In recent years, antimicrobial nanomaterials have emerged to prevent resistant infections.<sup>7–9</sup> Silver (Ag) nanoparticles have demonstrated broad-spectrum antimicrobial activity.<sup>10–12</sup> However, bacterial proteins induce the coagulation of these nanoparticles, hence thwarting their efficacy.<sup>13–15</sup> To address this problem, the functionalization of these nanoparticles has been proposed. However, the functionalization can negatively affect the antibacterial activity of the nanoparticles.<sup>16–18</sup>

Highly ordered arrays of self-assembled coordination polymers with a metal coordination center have demonstrated potent antimicrobial properties.<sup>11,19–21</sup> They have also shown long-lasting antibacterial activity because they can act as a

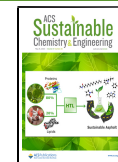
biocidal reservoir that releases biocidal metal ions gradually.<sup>11,22</sup> Because the antimicrobial properties of coordination polymers depend on both the nature of the organic linker and that of the metal center, a variety of antibacterial networks can be designed and synthesized.<sup>20,23–25</sup>

In many cases, the synthesis of supramolecular structures requires long reaction times, hazardous solvents, and high temperatures, thus limiting their industrial applications.<sup>26,27</sup> It is, therefore, necessary to develop facile, rapid, inexpensive, and environmentally friendly techniques for preparing these structures. An ambient temperature synthesis via rapid precipitation is a viable strategy to promote the widespread application of these compounds. Furthermore, the use of water

Received: January 8, 2020

Revised: April 23, 2020

Published: May 1, 2020



as the reaction medium instead of hazardous solvents lowers the cost, negative environmental impacts, and safety risk of the synthesis.<sup>28</sup>

A variety of multidimensional networks can be created, as there are many different metal ions and organic linkers, and the structure and properties of coordination polymers depend on the type of metal ions and organic linkers that the polymers are made from. Several linkers have been used to synthesize silver-based coordination polymers. However, to the best of our knowledge, the preparation of silver-based coordination polymers from imidazole, 2-methyl imidazole, or benzimidazole with green solvents at room temperature has not been reported yet.<sup>20,24,29</sup> The antibacterial, antiviral, and antifungal activity of imidazole linkers and their derivatives have been reported in the literature.<sup>30–33</sup> Here, taking advantage of the antimicrobial properties of the diazole-containing ligands and of Ag as the most well-known biocidal metal center, we report the design and synthesis of three new Ag-based metal–azolate frameworks (Ag-MAFs). The imidazole-based linkers (imidazole, 2-methyl imidazole, and benzimidazole) have different chemistries. Incorporating these antimicrobial ligands into biocidal metal centers has allowed for the creation of a class of nanosized Ag-based MAFs that offer high antimicrobial properties. Indeed, the antimicrobial activity in these systems originates from the synergistic antibacterial effects of both metal center and organic linker. The production of these nanomaterials is performed via a facile and environmentally friendly method at room temperature. Specifically, the synthesis is carried out in aqueous systems, in the absence of any hazardous solvents, and with low energy consumption. The produced Ag-MAFs are characterized thoroughly, and their antibacterial properties are evaluated with model bacteria using fluorescence imaging and flow cytometry.

## EXPERIMENTAL SECTION

**Materials.** Silver nitrate ( $\text{AgNO}_3$  >99%), 2-methylimidazole (>99%), imidazole (>99%), benzimidazole (>98%), and ethanol (>99%) were purchased from Merck, Germany. *Escherichia coli* (ATCC 35695) and *Bacillus subtilis* (ATCC 23857) were used as Gram-negative and Gram-positive model systems, respectively. LB broth with agar (Sigma-Aldrich; cat. no.: L2897) and Terrific Broth (TB, Sigma-Aldrich; cat. no.: T0918) were used for bacterial cell culturing. Propidium iodide (Sigma-Aldrich) and SYTO9 (Molecular Probes) were used for bacterial staining.

**Synthesis of Ag-MAFs.** For the preparation of the metal solution, 0.17 g (1.0 mmol) of  $\text{AgNO}_3$  was dissolved in 30 mL of deionized water. For the preparation of the ligand solutions, 0.082 g (1.0 mmol) of 2-methylimidazole, 0.068 g (1.0 mmol) of imidazole, and 0.118 g (1.0 mmol) of benzimidazole were separately dissolved in 30, 25, and 40 mL of ethanol, respectively. Next, all the solutions were homogenized by sonication for 2 min. The three ligand solutions were then gradually added to separate  $\text{AgNO}_3$  solutions while stirring at room temperature. Each mixture was stirred for another 30 min to complete the reaction. The precipitate was recovered, washed with fresh ethanol and deionized water several times, and finally air-dried. Figure 1 summarizes the synthesis process and depicts the molecular structures of the three Ag-MAFs, Ag-2-methylimidazole, Ag-Imidazole, and Ag-benzimidazole, which are referred to as Ag-2Imid, Ag-Imid, and Ag-Benz, respectively.

**Characterization of Ag-MAFs.** Attenuated total reflection–Fourier transform infrared (ATR-FTIR) spectroscopy (Varian Excalibur FTS-3000, with 16 scans and a resolution of  $4 \text{ cm}^{-1}$ ) was performed to determine the functional groups of the structures. To identify the crystalline structure of compounds, the samples were characterized by X-ray diffraction (XRD): XRD patterns were obtained at 298 K via an X’Pert-Pro X-ray diffractometer equipped

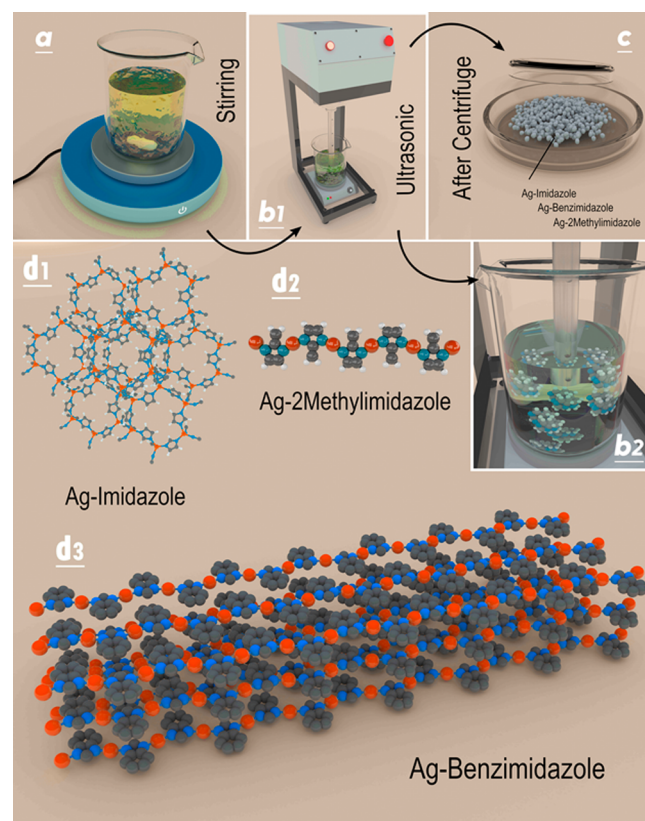


**Figure 1.** Photos showing the steps of the Ag-MAFs synthesis process: (a) solution preparation and stirring, (b<sub>1</sub>, b<sub>2</sub>) washing process, and (c) nanoparticle powder obtained after centrifugation. (d<sub>1</sub>–d<sub>3</sub>) Images depicting the Ag-MAFs molecular structures (silver, carbon, nitrogen, and hydrogen atoms are shown in red, black, blue, and white, respectively).

with a  $\text{Cu K}\alpha$  radiation source ( $\lambda = 1.5406 \text{ \AA}$ ) at 40 mA and 40 kV. The morphology of the samples was analyzed via field emission scanning electron microscopy (FE-SEM, MIRA3 TESCAN) equipped with energy-dispersive X-ray (EDX) spectroscopy, and via transmission electron microscopy (TEM, Zeiss EM900) operated at 20 kV. The average size distributions of nanomaterials were determined via dynamic light scattering (DLS, Nano ZS ZEN 3600). Prior to measurements, the samples were sonicated in water. The zeta potentials of the nanoparticles were measured with ZetaPALS (Brookhaven Instruments) at a pH of 6 with 1 mM KCl, whereby the average of five trials with 30 cycles per run is reported. The absorption spectra of the nanoparticles were determined via a UV–Vis spectrophotometer (PerkinElmer LAMBDA 35). X-ray photoelectron spectroscopy (XPS) (Bestec, Germany) equipped with a 100  $\mu\text{m}$  monochromatic Al  $\text{K}\alpha$  X-ray photoelectron spectrometer source was used to determine the characteristic elements of the structures, where a hemispherical electron energy analyzer was used to record the emitted photoelectrons.

**Bacterial Strains and Suspension Preparation.** Antimicrobial properties of the nanomaterials were evaluated using the Gram-negative *E. coli* and Gram-positive *B. subtilis* species. The bacterial strains were cultivated on LB agar medium plates at 37 °C for 24 h and then stored at 4 °C for future use. A discrete colony of each bacterial strain was grown aerobically at 37 °C in TB culture media in a shaking flask at 150 rpm for ~10 h (at middle-to-late exponential phase). After centrifuging at 1500g for 2 min, the pellet of cultured bacteria was gently washed three times with phosphate buffer saline, PBS (pH = 7.3), to remove the residual TB. A Rotamix (10101-RKVSD, ATR Inc.) at 20 rpm was used to resuspend the pellet cells in PBS. Bacterial stock samples with cell densities of  $\sim 2 \times 10^8 \text{ cfu/mL}$

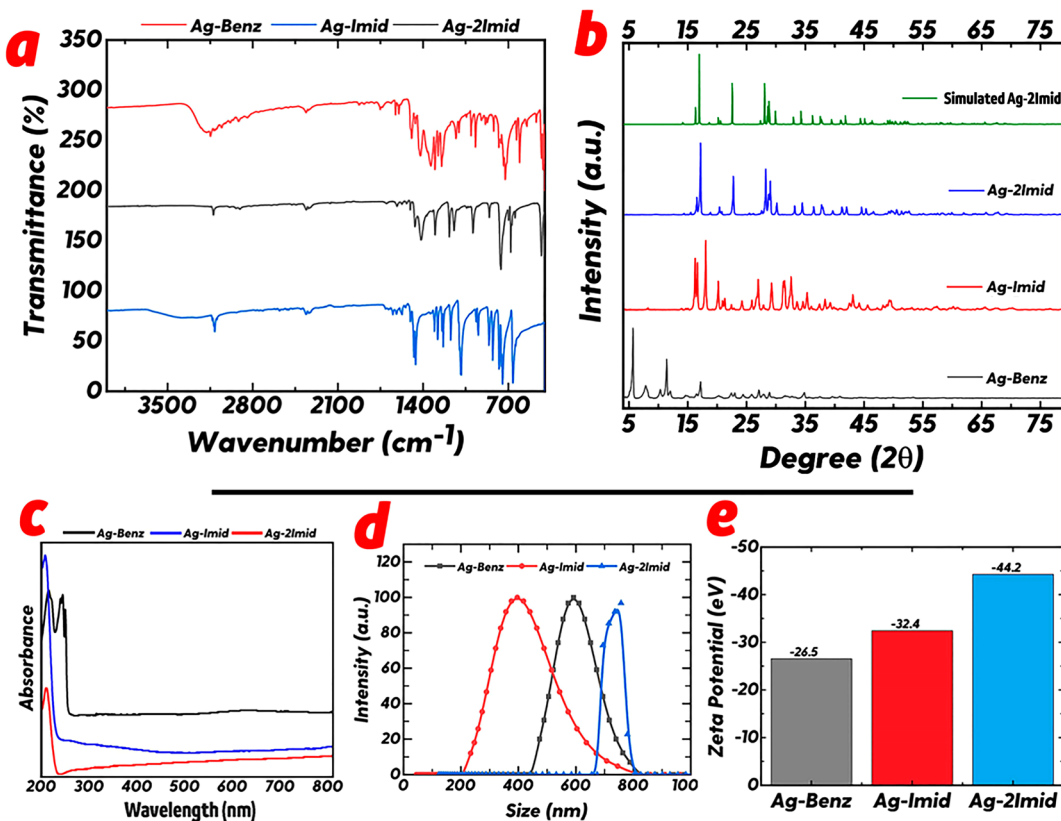


Figure 2. (a) ATR-FTIR spectra, (b) XRD patterns, (c) UV-Vis spectra, (d) DLS results, and (e) zeta potentials of Ag-MAFs.

were prepared from each cultivated colony to be used for antibacterial assessment.

**Fluorescence Imaging of Bacteria.** Stock suspensions of the Ag-MAF nanostructures with a concentration of 400  $\mu\text{g}/\text{mL}$  were prepared in 10% dimethyl sulfoxide (DMSO). For treated samples, bacterial stock samples were exposed to a final concentration of 200  $\mu\text{g}/\text{mL}$  of each Ag-MAF structure for 3 h (with a final concentration of 5% DMSO). To examine the possible impact of DMSO on bacterial survival, DMSO with a final concentration of 5% was added to the untreated bacterial samples. The untreated and treated samples were subsequently incubated with 20  $\mu\text{M}$  of propidium iodide and 5  $\mu\text{M}$  of SYTO9 for 15 min in the dark at room temperature. To avoid osmotic stress on bacterial samples, the propidium iodide/SYTO9 solution was prepared in a PBS solution. A 20  $\mu\text{L}$  aliquot of each sample was added onto a microscope glass slide, enclosed by a glass coverslip. The glass slide was then placed on the microscope stage (Nikon ECLIPSE TE200 microscope). Epifluorescence images of at least 15 field-of-view (i.e., Exc./Det. of 560/630 for propidium iodide and 480/535 for SYTO9) were recorded for each sample, and more than 2000 cells were counted for three separate trials. The ratio of the areas of propidium iodide-stained cells (red) to SYTO9-stained cells (green) were used to estimate the percentage of dead bacteria in each sample. Image analysis was performed by using ImageJ software (National Institutes of Health, 1.43u). Welch's *t*-test was used to analyze the statistical differences ( $\alpha = 0.05$ ) between the proportion of live cells in the untreated samples and in the samples treated with each of the three Ag-MAFs.

**Flow Cytometry of Bacteria.** Treated or untreated samples (100  $\mu\text{L}$ ) (see above) were added into a 96-well flat-bottom plate and incubated with 20  $\mu\text{M}$  propidium iodide in PBS for  $\sim 15$  min in complete darkness. Flow cytometry analyses were conducted with a medium fluid rate and the limit of 100,000 events for each trial. To remove debris impact, two thresholds were applied before the analyses in which only forward angle scattering height (FSC-H) signals larger than 10,000 and side-angle scattering height (SSC-H) signals larger than 100 were collected. The propidium iodide molecule

was illuminated with a 15 mW argon ion laser (488 nm), and fluorescence signals were recorded via the FL2 channel with a detection wavelength of  $585 \pm 40$  nm. The fluorescence signals were amplified with the logarithmic mode and shown on the logarithmic scale. To perform single-cell analysis, a FSC-H versus FSC-A (-area) counterplot was used to remove doublets from our calculations in which the doublets show a separate population toward higher-area values. Three separate flow cytometry experiments were performed for each bacterial suspension. The flow cytometry data were analyzed by the BD Accuri C6 software. Statistical comparisons were conducted between the proportion of live bacteria treated with two of the Ag-MAFs (e.g., Ag-Benz vs. Ag-Imid for *E. coli*). The null hypothesis for each comparison was "no difference in the proportion of bacteria living". The two-tailed *P*-values from Welch's *t*-test were used to evaluate the statistical significance.

## RESULTS AND DISCUSSION

**Characterization of Ag-MAFs.** To investigate the important parameters affecting the biocidal properties of the Ag-MAFs, their morphology and surface chemistry were carefully evaluated. Generally, N-heterocyclic carbene (NHC)-metal complexes can be prepared by direct metalation. NHCs can form strong bonds to a wide range of metals because of their excellent  $\sigma$ -donor and weak  $\pi$ -acceptor ability. NHCs coordinate to metal ions via  $\sigma \rightarrow \text{d}$  donation.<sup>34</sup> Because main-group elements and rare-earth metals lack  $\pi$ -back-donation while NHCs have a pure  $\sigma$ -donor character, the latter forms stable adducts with the metal centers.<sup>35</sup> On account of the flexibility of NHC ligands, they can form stable electron-deficient metals via a  $\pi \rightarrow \text{d}$  donation and stabilize electron-rich metals by  $\text{d} \rightarrow \pi^*$  back-donation.<sup>36</sup> Fundamentally, the integration of steric and electronic characteristics of an NHC in a specific coordination environment affects the stability of the carbene lone pair. From the structural

perspective, the bulkiness of the bonded groups to the nitrogen atoms of the NHCs and the short metal–carbon distances in their metal complexes improve the steric congestion around the metal center. The NHC–metal bond is formed by the Coulombic attraction between the lone-pair electrons at the carbene sites and the positively charged metal atoms. Also, there are considerable covalent interactions originated by the donor lone-pair electrons. In this regard, a DFT study conducted on the NHC–metal bonding of a series of Ag–NHCs complexes confirmed that the NHCs have good-donating but relatively weaker-accepting characteristics,<sup>37</sup> while the electron donation of the NHC carbene lone pair occurred at an unfilled p (5p) or s (5s) orbital of the Ag atoms.

Among various ligands used for supramolecular silver-based building blocks, multidentate building blocks containing a nitrogen (N) donor based on imidazole can lead to morphologically promising architectures. The  $\text{Ag}^+$  ion has a great affinity to N-donor ligands and reacts with these linkers via coordination bonds, hence creating metal coordination supramolecular structures. Regardless of potential applications of their coordination compounds in biomedical chemistry,<sup>38</sup> the coordination chemistry of the imidazole containing ligands has not been studied in detail and a few complexes have been reported in the literature.<sup>39–41</sup> The presence of the imidazoline moiety with well-known biocidal activity in the structure of organic linkers makes them promising candidates for antimicrobial studies.<sup>30–32</sup> Thanks to the synergetic presence of  $\text{Ag}^+$  ions and azole rings in the structure of Ag-based MAFs, they represent promising antimicrobial agents against Gram-positive and Gram-negative bacteria.

To validate the coordination of silver and imidazole-based ligands, as well as the chemical structures of Ag-MAFs, FTIR analysis was performed and the results are presented in Figure 2a. Signals appearing in the IR spectrum of the Ag-2Imid structure were consistent with those previously reported for 2-methylimidazole compounds.<sup>42,43</sup> The peaks observed at 3135 and 2924  $\text{cm}^{-1}$  can be associated with the aliphatic and aromatic asymmetric C–H stretching, respectively.<sup>42–44</sup> The band observed at around 1580  $\text{cm}^{-1}$  corresponds to the C=N stretching vibration in imidazole structure.<sup>42</sup> The bands at around 1144, 992, 760, and 1610  $\text{cm}^{-1}$  are attributed to the C–N stretching, C–N bending, C–H bending, and C=C stretching vibrations, respectively.<sup>45,46</sup> Moreover, the peaks around 1300–1465  $\text{cm}^{-1}$  correspond to the entire ring stretch of the imidazole group.<sup>42,47</sup>

In the case of Ag-Benz, there is a sharp peak at around 3135  $\text{cm}^{-1}$  because of the C–H stretching vibration. Although there are several N–H signals between 3335 and 2500  $\text{cm}^{-1}$  (the Aldrich Library of FTIR Spectra, ed II, vol. 3), all these peaks disappeared after the coordination with Ag atoms, indicating benzimidazole linkage to the framework of Ag-Benz.<sup>48</sup> Moreover, two peaks around 1608 and 1580  $\text{cm}^{-1}$  can be associated with C=C and C–N vibrations, respectively.<sup>46</sup> The absorption band at 769  $\text{cm}^{-1}$  in the Ag-Benz spectrum is related to the typical out-of-plane C–H bending vibration of ortho-disubstituted benzene in the benzimidazole linker.<sup>46,49</sup>

Compared to the control imidazole for which different signals exist between 2500 and 3335  $\text{cm}^{-1}$ ,<sup>50</sup> the disappearance of almost all of these peaks indicates that imidazole molecules were coordinated with Ag atoms and connected to the backbone of Ag-Imid.<sup>48</sup> Meanwhile, the peaks appeared at about 3018, 659, and 1541  $\text{cm}^{-1}$  can be ascribed to the N–H

stretching, out-of-plane NH<sub>2</sub> bending, and N–H bending vibrations of imidazole, respectively.<sup>50</sup>

The crystalline structure and crystalline phase of the metal–organic complexes have been determined by XRD characterization, as shown in Figure 2b. The XRD patterns of Ag-Imid and Ag-Benz suggest the formation of their crystalline planes. The sharpest peaks with the highest intensity in the XRD pattern of Ag-2Imid indicate its higher crystallinity compared with the other samples. Based on a calculation with a peak-position error of less than 0.02°, a crystalline unit cell in the form of a monoclinic lattice (based on Bravais Lattice category) is proposed for Ag-Imid by adapting the XRD data with ITO15 program, while  $\beta = 90.71^\circ$  was calculated.<sup>51</sup> In this regard, the peaks at 16.34, 17.75, 19.88, and 28.96° can be attributed to (011), (012), (013), and (203) crystal planes, respectively. In a similar way, a triclinic lattice by the use of DIKVOL91 program is proposed for the Ag-Benz crystalline structure, for which the main peaks at 5.67, 7.84, 11.41, and 17.17° can be associated with (011), (111), (122), and (213) crystal planes, respectively.<sup>52</sup> The XRD pattern of Ag-2Imid demonstrates several highly sharp peaks at  $2\theta = 16.89, 22.47, 27.98$ , and  $28.78^\circ$ , which can be assigned to (011), (200), (211), and (013) crystal planes based on the ITO15 program. The crystal structure of Ag-2Imid has already been reported.<sup>53</sup> The XRD pattern we obtained in our study exactly matches with the simulated XRD pattern extracted from the CIF file reported in ref 53. In the other words, the peaks are notably consistent with the pattern calculated from the primitive monoclinic unit cell structure reported by Huang et al.<sup>53</sup> This indicates that the Ag-2Imid crystals were formed perfectly via the procedure applied in this study. Therefore, we propose the same crystal structure for Ag-2Imid, that is, one-dimensional (1D) zigzag chains where two Ag(I) centers giving rise to the absolute 180° of N–Ag–N angles and the antiarrangement of neighboring 2-methylimidazolate rings (Figure S1).

UV–Vis spectroscopy was also performed to corroborate the results discussed above. The absorption spectra of nanostructures are presented in Figure 2c. On account of the presence of conjugated  $\pi$  bonding ( $\pi$ – $\pi^*$  transition) and nonbonding electron (n– $\pi^*$  transition) systems, imidazole derivatives absorb UV light because there are definite energy gaps between  $\pi$ – $\pi^*$  and n– $\pi^*$  orbitals.<sup>50</sup> Regarding the UV–Vis spectra of the Ag-2Imid and Ag-Imid, there is an insignificant difference between these two samples because of the structural similarity of the linkers. The characteristic absorption peaks of these Ag-MAFs were observed at  $\lambda_{\text{max}}$  of 208 nm, whereby a hypsochromic shift in maximum absorbance was observed. On the contrary, Ag-Benz showed both hypsochromic and bathochromic effect at the maximum absorbance ( $\lambda_{\text{max}}$  of 215 nm), which may be ascribed to the charge and energy-transfer difference between the imidazole and benzimidazole molecules.

As illustrated in Figure 2d, the results of DLS analysis indicate that Ag-2Imid, Ag-Imid, and Ag-Benz MAF nanostructures mainly exhibited an average size distribution of 760, 400, and 550 nm, respectively, which is in agreement with the FE-SEM and TEM images. Because surface charge of Ag-MAFs affect their properties, zeta potential measurements were also carried out. As illustrated in Figure 2e, all the Ag-MAF nanostructures showed a negative charge around neutral pH. However, Ag-2Imid showed the highest negative surface charge, while Ag-Benz demonstrated the lowest negative surface charge. It is important to underline that bacterial

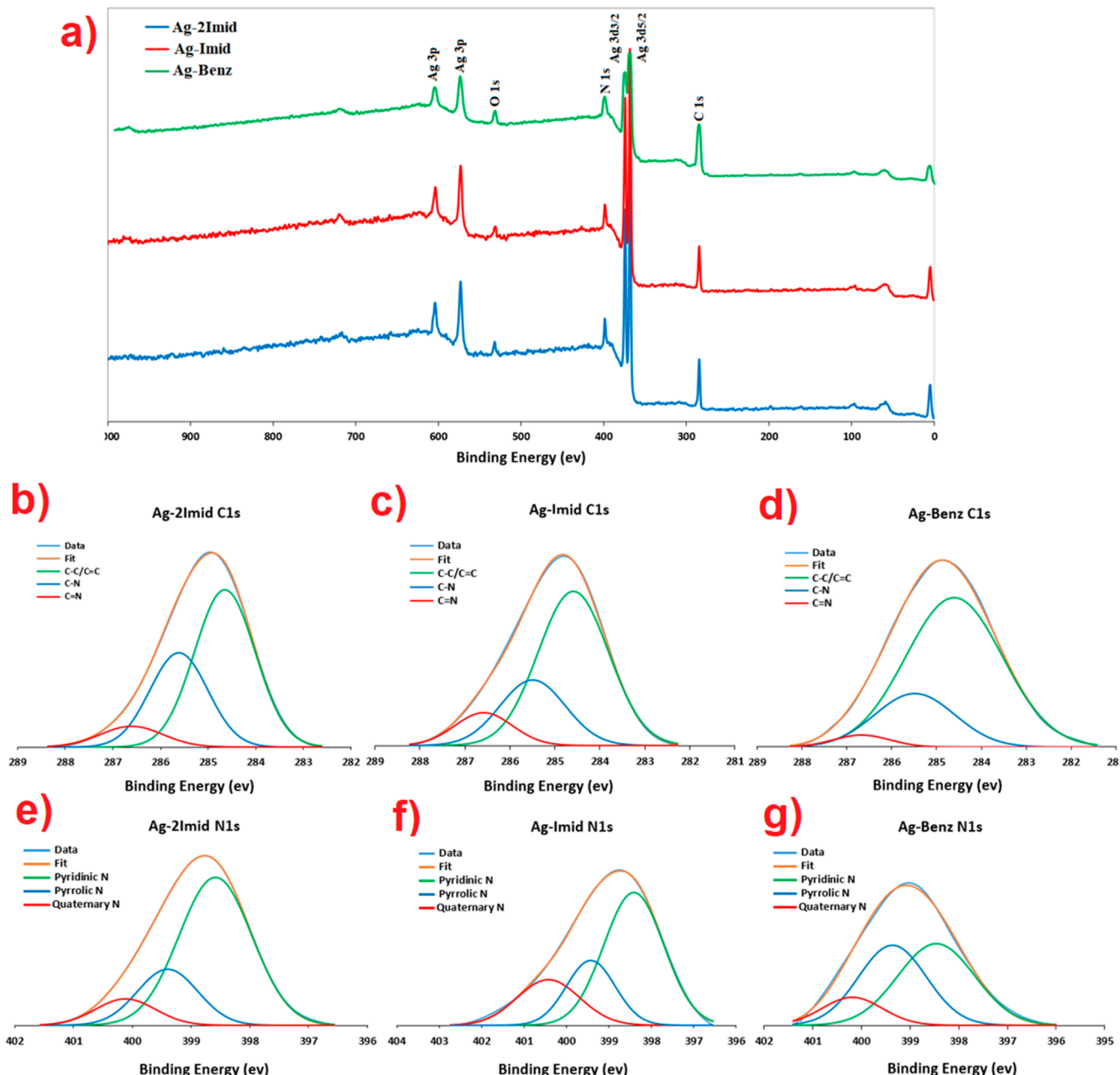


**Figure 3.** (a) XPS survey spectra of the Ag-MAFs and the deconvoluted high-resolution spectra of (b) C (1s) of Ag-2Imid, (c) C (1s) of Ag-Imid, (d) C (1s) of Ag-Benz, (e) N (1s) of Ag-2Imid, (f) N (1s) of Ag-Imid, and (g) N (1s) of Ag-Benz of the Ag-MAFs.

cells are normally negatively charged in a pH range of 4–9,<sup>54,55</sup> thus, the negative potential of the Ag-MAFs can provide electrostatic repulsion to bacteria.<sup>56</sup>

XPS was performed to determine the elemental composition and chemical structure of the synthesized Ag-MAFs (Figure 3). The survey spectra of Ag-MAF nanostructures principally included the energy peaks related to carbon (C), nitrogen (N), and silver (Ag) elements (Figure 3a). The elemental compositions of all Ag-MAFs are listed in Table 1, comprising the amplitude of the O (1s), N (1s), C (1s), Ag 3d<sub>5/2</sub>, and Ag 3d<sub>3/2</sub> peaks, which are located at around 532, 399, and 285, 368, and 374 eV, respectively.<sup>57</sup> The presence of silver signals clearly indicates the formation of Ag-based MAFs. The highest and lowest contents of silver atoms were observed for Ag-2Imid and Ag-Benz, respectively.

**Table 1. Elemental Compositions of the Ag-MAFs**

nanoparticle	atomic concentration (%)				
	C (1s)	O (1s)	N (1s)	Ag (3d)	Ag (3p)
Ag-2Imid	33.55	4.60	34.15	15.40	12.30
Ag-Benz	49.25	4.20	30.35	9.10	7.10
Ag-Imid	27.40	7.10	38.50	14.70	12.30

More information on the chemical coordination of the Ag-MAF nanostructures can be extracted by the deconvolution of the C 1s and N 1s high-resolution spectra (Figure 3b–g). The result for C 1s includes two main peaks: a major peak located at 284.6 eV, which is assigned to the C–C/C=C bond,<sup>58</sup> an intermediate peak at 285.6 eV attributed to the C–N bond,<sup>9,10</sup> and a minor peak at 286.5 eV assigned to the C=N bond.<sup>59</sup> In view of the structures of 2-methylimidazole, benzimidazole,

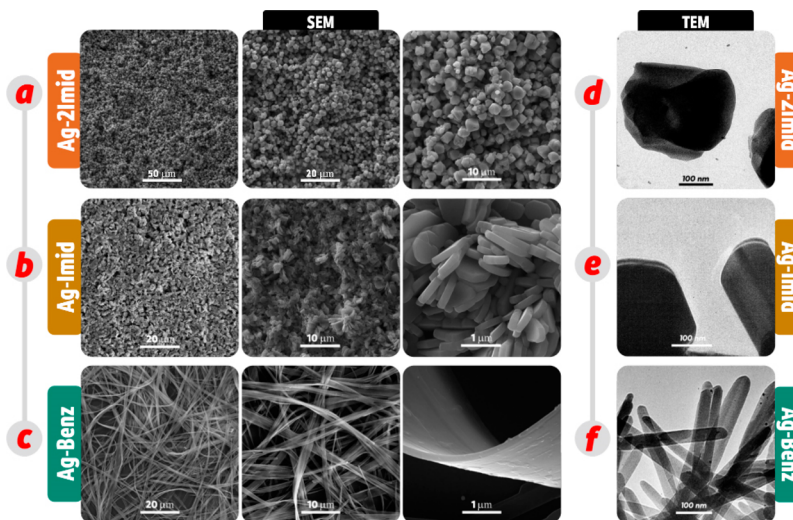


**Figure 4.** Representative FE-SEM and TEM images of Ag-MAF nanostructures at different magnifications: (a–c) FE-SEM and (d–f) TEM images of Ag-2Imid, Ag-Imid, and Ag-Benz are in the form of octahedral nanocrystals, hexagonal nanostructures, and nanoribbons, respectively.

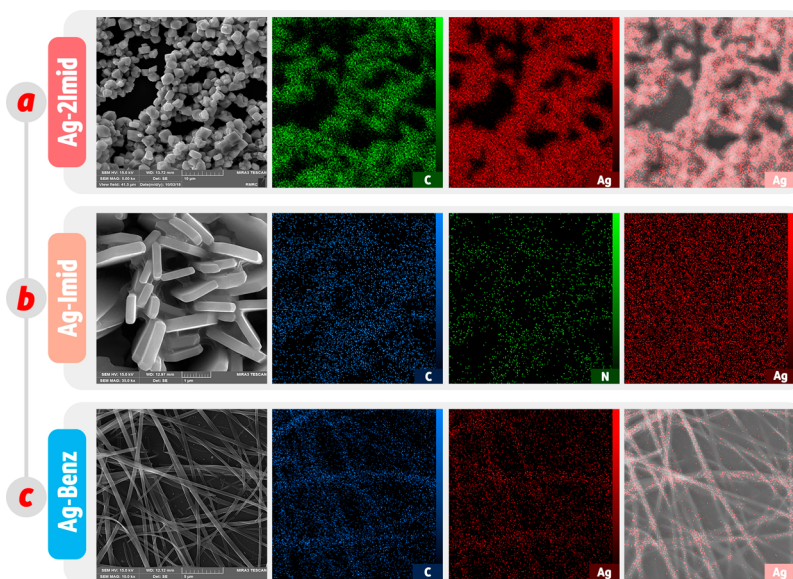


**Figure 5.** (a–c) FE-SEM images and EDX-mapping of the Ag-2Imid, Ag-Imid, and Ag-Benz structures, respectively.

and imidazole ligands applied for the synthesis of Ag-MAFs, mainly three kinds of nitrogen-containing functional groups can be observed in all these organic linkers, namely, pyridinic-N, pyrrolic-N, and quaternary N centers.<sup>60,61</sup> Indeed, the N 1s spectra of Ag-MAFs comprised three main peaks: a peak located around 398.6 eV corresponding to the imidazole = N– bond (pyridinic-N of imidazole-based linkers), a peak around 399.4 eV associated with the –NH– bond (pyrrolic-N groups of the linkers), and another peak at 400.1 eV attributed to the quaternary N centers after reaction with Ag atoms. This new peak formed can be assigned to the protonated N atoms coordinated with Ag.<sup>60–63</sup> Indeed, all Ag-MAF structures form polymeric structures in which the silver atoms are coordinated with the deprotonated amine N of one imidazolate ligand and the imine nitrogen of a neighboring imidazolate ligand.

To further confirm the successful formation of nanoscale Ag-MAFs and investigate their structures, several morphological characterizations including FE-SEM and TEM were conducted (Figures 3 and 4). As can be observed in Figure 4a, the

synthesized Ag-2Imid consisted of octahedral nanocrystals with an average particle size distribution of 200–700 nm and no obvious agglomeration was observed. Figure 4b indicates that Ag-Imid has a hexagonal nanostructure with a thickness mainly distributed in the range of 250–350 nm (Figure S2). The length of these hexagonal nanostructures fell in the range of 400–800 nm (Figure 2d). Finally, the Ag-Benz nanostructures are in the form of nanoribbons, with an average thickness of 160–190 nm (Figure 4c), while their width mainly fall in the range of 200–500 nm (Figures 2d and S2). The TEM results (Figure 4d–f) were in agreement with the FE-SEM images, indicating two-dimensional (2D) nanoribbons and hexagonal nanostructures for Ag-Benz and Ag-Imid MAFs, respectively.

Regarding the XRD patterns and FE-SEM images, it could be inferred from the fact that the morphologies of Ag-MAFs mainly depend on their crystal structure.<sup>64–66</sup> Imidazole-based ligands are great candidates to form self-assembled coordination polymers.<sup>67</sup> The polymeric structure shown in Figure 1 is

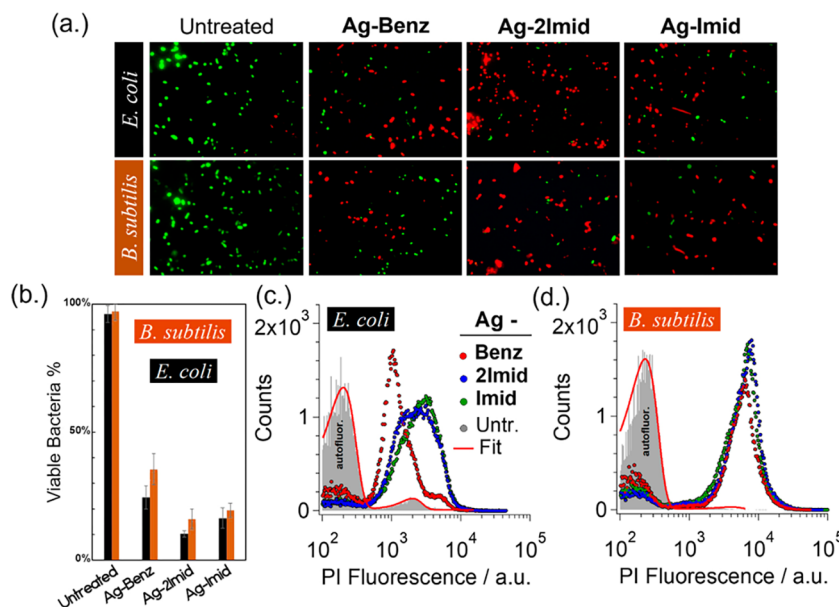


**Figure 6.** Antibacterial activity of the Ag-MAFs against *E. coli* and *B. subtilis* investigated by fluorescence imaging and flow cytometry techniques. The bacteria were exposed or not exposed (“untreated”) to 200  $\mu\text{g}/\text{mL}$  of Ag-Benz, Ag-Imid, and Ag-2Imid for 3 h. (a) Fluorescence images of the samples stained with propidium iodide/SYTO9 present the relative population of dead (damaged) cells in each field-of-view. (b) Percentage of viable cells obtained from four independent confocal microscopy experiments for each bacterial strain; error bars represent  $\pm$  one standard deviation. (c,d) Flow cytometry histograms of the propidium iodide-stained samples show two separate regions: bacterial autofluorescence and propidium iodide-enhanced fluorescence (dead cells).

proposed to represent the hexagonal nanosheets of Ag-Imid. In this structure, each  $\text{Ag}^+$  center is coordinated with four imidazole ligands in a tetrahedral geometry, leading to the formation of hexagonal sheets made from hexanuclear rings. Similar hexanuclear units and more examples of related structures formed by imidazole-based ligands have already been reported.<sup>67–70</sup> To represent the structure of the long-chain nanoribbons of Ag-Benz indicating the one-dimensional feature of this compound, we proposed the infinite structure shown in Figure 1. In this structure, each  $\text{Ag}^+$  center is coordinated with two benzimidazole ligands, and the ligands act as a bridging unit between two adjacent  $\text{Ag}^+$  ions, leading to the formation of 1D infinite coordination polymers. This 1D zigzag structure for Ag-Benz complex was also proposed in ref.<sup>71</sup> in which the structural details of a series of  $\text{Ag}^+$  complexes of substituted imidazoles were discussed. Weak intermolecular interactions (hydrogen bonding and  $\pi-\pi$  interactions) between imidazole rings play an important role in constructing 2D assemblies from 1D chains.<sup>72–77</sup> Therefore, the 2D morphology of the nanoribbons of Ag-Benz could be due to the connection between a series of parallel 1D chains linked via intermolecular interactions.<sup>78</sup>

All EDX spectra (Figure 5) from the Ag-MAFs nanostructures confirmed that the nanostructures were mainly composed of carbon (C), nitrogen (N), and Ag atoms, all detected in sharp peaks. The oxygen (O) peaks are mainly related to absorbed water. More importantly, the morphological texture of Ag-MAFs revealed the homogeneous distribution of C, N, and Ag atoms across the entire nanostructures (Figures S3 and S4). The octahedral nanocrystals of Ag-2Imid, nanoribbons of Ag-Benz, and hexagonal nanostructures of Ag-Imid can also be recognized by their corresponding SEM images in Figure 5.

**Antibacterial Properties of Ag-MAFs.** Among various strategies suggested to examine the viability of bacterial cells subjected to external stimuli, propidium iodide staining has

frequently been used to assess the integrity of bacterial membranes.<sup>79,80</sup> Propidium iodide is a fluorescent molecule that exhibits a fluorescence enhancement of  $\sim$ 30-fold upon intercalation into double-stranded regions of DNA.<sup>81,82</sup> Given that the cytoplasmic membrane (CM) of bacterial cells are impermeable to propidium iodide and that bacterial DNA is found exclusively within the cell cytosol, propidium iodide fluorescence enhancement is observed only if the integrity of the CM has been lost. Specifically, breakdown-induced permeability enhancement of the bacterial CM results in the uptake of propidium iodide, followed by fluorescence increment. The SYTO9 molecule, on the other hand, can readily be transported across the intact CM. Using both fluorescent probes allows the evaluation of the ratio of dead/live cells in a bacterial sample (i.e., propidium iodide-stained for dead; SYTO9-stained for live). Flow cytometry and fluorescence imaging are usually applied as complementary techniques to evaluate the viability of bacterial cells exposed to an antimicrobial treatment<sup>83</sup> or antibacterial nanomaterials.<sup>6,84</sup> While fluorescence imaging allows visualizing the percentage of dead cells in a small bacterial population, flow cytometry provides statistical results over a high population of the cells (e.g., 100,000 cells).

Figure 6 summarizes fluorescence imaging and flow cytometry results obtained with *E. coli* and *B. subtilis* bacteria species after exposure to 200  $\mu\text{g}/\text{mL}$  of Ag-MAFs for 3 h. The majority of bacteria in the control samples were stained only with SYTO9 molecules (i.e.,  $>95\%$ ); see Figure 6a,b. The Ag-MAF-exposed samples, however, showed a high-density population of cells stained with the propidium iodide. The strong antibacterial properties of the Ag-MAF nanostructures are reflected in the significant decline of the viable *B. subtilis* bacteria from a percentage of 97.3% (untreated) to 35.5, 19.5, and 16.1% in Ag-Benz, Ag-Imid, and Ag-2Imid-exposed samples, respectively. A similar trend was observed for *E.*

*coli*, for which the fraction of viable population was significantly decreased from 96.2% (untreated) to 24.5, 16.4, and 10.3% in samples exposed to Ag-Benz, Ag-Imid, and Ag-2Imid, respectively (Figure 6d). All Ag-MAF-treated samples had significantly fewer living *E. coli* and *B. subtilis* cells than the untreated samples. Comparison between the Ag-MAF-treated samples revealed first that the Ag-2Imid- and Ag-Imid-exposed samples had significantly fewer living *E. coli* and *B. subtilis* cells than the Ag-Benz ( $P < 0.01$  for all comparisons). Comparison between Ag-2Imid-exposed samples and Ag-Imid were less conclusive; while Ag-2Imid had a lower mean number of living cells than Ag-Imid, the difference was statistically significant only for *E. coli* and not *B. subtilis*.

Figure 6c,d shows complementary findings obtained with the flow cytometry technique. Two distinct regions can be observed in the propidium iodide fluorescence histogram of the untreated samples, that is, negative control samples that were not exposed to the Ag-MAFs. The low-signal region (1 to  $5 \times 10^2$ ) resulted from the bacterial autofluorescence (and free propidium iodide molecules), depicted by a background gray histogram. On the other hand, the population with a fluorescence of  $>5 \times 10^2$  corresponds to the propidium iodide-stained cells (cells with disrupted CM). Considering that the flow cytometry measurements are accompanied by the same limit of 100,000 events, the percentage of damaged cells in each sample was simply calculated from the number of detected cells in the two distinct populations. Although the center of the dead cells histogram in the Ag-Benz-exposed *E. coli* sample was shifted to lower fluorescence intensities, the whole population was still in the region of  $>5 \times 10^2$  values. For this Ag-MAF, fewer propidium iodide molecules were able to pass through the damaged CM.

The histograms of the Ag-MAF-treated samples of *B. subtilis* are all centered at  $\sim 10^4$  values, revealing that the three nanostructures disrupted the CM almost equally. To perform an unbiased statistical analysis of the flow cytometry results, we first fitted the flow cytometry signals of untreated samples to a double-Gaussian distribution equation (fitted lines in Figure 6c,d). The first Gaussian plot is assigned to the live cell population and the second plot refers to the cells with PI-permeable CMs. The untreated signals were used as constraints to obtain a PI fluorescence threshold of live/cell regions. For example, in *E. coli* samples, a threshold of 800 (i.e., with an arbitrary unit) was applied to the treated samples in which signals above the value of 800 were resulted from PI-stained cells (dead cell), whereas signals below 800 were resulted from autofluorescence of the bacterial cells. The threshold for *B. subtilis* bacteria occurred at higher fluorescence signals of  $\sim 1200$ . The percentage of viable bacterial cells in each sample was calculated from the cell population in the two Gaussian regions. The flow cytometry results illustrated in Figure 6c,d agreed well with the confocal fluorescence microscopy results in Figure 6d.

The Ag-MAF-induced changes in the bacterial cells were mainly due to increased permeability of the CM rather than disruption of the entire cell. Despite the low particle-to-cell ratio of  $\sim 2$  pg/cell, the antibacterial activity of the nanostructures was observed during the first 3 h of experiments.

Likely antimicrobial mechanisms can be proposed for the Ag-MAFs. Silver-containing hybrid organic–inorganic materials have a well-known reputation as biocidal tools owing to their strong antibacterial property and high durability.<sup>85</sup>

Besides, Ag-based metal–organic framework (MOFs) have been reported as antibacterial materials.<sup>86</sup> The toxicity and antimicrobial mechanism of action of Ag-containing materials can be related to the Ag ions' coordination ability to N, O, or S donor atoms, and hydroxyl, carbonyl, carboxyl, amino, and sulphydryl functional groups present in DNA, or the bacterial cell membrane, resulting in biological deactivation of bacteria.<sup>85,87,88</sup> It is worth mentioning that Ag<sup>+</sup> ions can also infiltrate into a bacterial membrane and deteriorate cell membrane integrity.<sup>23,89</sup> Different possible mechanisms of action have been reported for metal-organic-based nanomaterials:

- The gradual release of the metal ions whether in the form of a cation or small fragments of the structure<sup>86,90</sup> is the most apparent reason for the toxicity of MOFs. In this case, the antimicrobial activity is directly proportional to the kinetics of cation release, and it increases with the density of released ions.<sup>86,90,91</sup>
- The intrinsic properties of the organic linker in the platform, as the organic linker might itself have antimicrobial activity.
- The crystal size of the nanostructure especially when it falls in the range of nanometer scales, as cells tend to incorporate nanostructures by endocytosis and pinocytosis.<sup>92</sup> In this regard, several recent reports have demonstrated that reducing the size of Ag nanoparticles could offer superior and wide-spectrum antimicrobial activity.<sup>93,94</sup>

Overall, the content of silver and nitrogen atoms in the structure of Ag-MAFs can provide a baseline indicator of their antibacterial activity. Despite the lowest repulsions between Ag-Benz and bacteria (zeta potential results), Ag-Benz presented the lowest silver and nitrogen concentrations (XPS), thus providing them with the lowest antibacterial activity among the synthesized Ag-MAFs. It has been suggested that morphological features also affect antimicrobial activity.<sup>95</sup> The sharp edges of Ag-2Imid crystal structures (as shown by SEM images) would allow the nanoparticles to better interact with bacterial cells. It is reported that the shape of an Ag nanoparticle strongly affects the antibacterial activity of the nanoparticle.<sup>96</sup> For example, triangular Ag nanostructures exhibited higher antibacterial activity than rod-shaped or spherical nanostructures.<sup>97</sup> A good nanostructure–bacteria interaction can induce a charge imbalance in the bacterial membrane, resulting in a surge of intracellular reactive oxygen moiety formation that kills bacterial cells. Consequently, the antibacterial activity can be controlled by modulating the Ag<sup>+</sup> release, the particle morphology, and the type of organic linker. Furthermore, the coordination strength of Ag-MAFs can affect the dissolution of silver and of the Ag-MAFs themselves. Molecules, such as cysteine, present in the structure of the subcellular molecules (proteins, enzymes, and DNA) of bacteria can induce the decomposition of Ag-MAFs. For instance, cysteine has been shown to induce the dissolution of zero-valent Ag nanoparticles via adsorption on the Ag nanoparticles surface, forming Ag–sulphydryl bonds.<sup>98</sup> Consequently, the release rate can be tuned using different organic linkers.

## CONCLUSIONS

In this study, we successfully synthesized three new Ag-MAFs with silver as the metal center coordinated with imidazole-

based linkers having different chemistries, via a facile and environmentally friendly method at room temperature. The imidazole-based linkers were chosen to investigate the effect of the linker chemistry on the antibacterial and structural properties of Ag-MAFs. The coordination of silver ions with 2-methylimidazole, imidazole, and benzimidazole led to the formation of octahedral, hexagonal sheet, and ribbon nanostructures, respectively. With their silver release and the imidazole groups, the Ag-MAFs showed excellent antibacterial activity in colloidal forms against *E. coli* and *B. subtilis*. Overall, the highest antibacterial activity was achieved for Ag-2Imid, likely owing to its higher silver concentration and specific nanocrystal structure. Ag-MAFs are novel antimicrobial nanostructures that may open a new avenue for antimicrobial applications.

## ASSOCIATED CONTENT

### Supporting Information

The Supporting Information is available free of charge at <https://pubs.acs.org/doi/10.1021/acssuschemeng.0c00201>.

1D zigzag chain formation in Ag-2-methylimidazole, FE-SEM images of Ag-MAFs, FE-SEM images and EDX mapping of Ag-2Imid structures, FE-SEM images and EDX mapping of Ag-Benz structures, and BET results of Ag-MAFs ([PDF](#))

## AUTHOR INFORMATION

### Corresponding Authors

**Ahmad Rahimpour** — *Department of Chemical Engineering, Babol Noshirvani University of Technology, Babol 4714781167, Iran; Department of Environment, Land and Infrastructure Engineering (DIATI) and Department of Applied Science and Technology, Politecnico di Torino, 10129 Turin, Italy; [orcid.org/0000-0003-1511-2761](#); Email: [ahmadrahimpour@nit.ac.ir](mailto:ahmadrahimpour@nit.ac.ir)*

**Mark A. Elliott** — *Department of Civil, Environmental and Construction Engineering, University of Alabama, Tuscaloosa, Alabama 35487, United States; [orcid.org/0000-0002-7835-0612](#); Email: [melliott@eng.ua.edu](mailto:melliott@eng.ua.edu)*

**Masoud Soroush** — *Department of Chemical and Biological Engineering, Drexel University, Philadelphia, Pennsylvania 19104, United States; [orcid.org/0000-0002-4879-5098](#); Email: [soroushm@drexel.edu](mailto:soroushm@drexel.edu)*

### Authors

**S. Fatemeh Seyedpour** — *Department of Chemical Engineering, Babol Noshirvani University of Technology, Babol 4714781167, Iran*

**Ahmad Arabi Shamsabadi** — *Department of Chemical and Biological Engineering, Drexel University, Philadelphia, Pennsylvania 19104, United States; [orcid.org/0000-0002-9726-2466](#)*

**Saeed Khoshhal Salestan** — *Department of Chemical Engineering, Babol Noshirvani University of Technology, Babol 4714781167, Iran; [orcid.org/0000-0001-6426-8389](#)*

**Mostafa Dadashi Firouzjaei** — *Department of Chemical and Biological Engineering and Department of Civil, Environmental and Construction Engineering, University of Alabama, Tuscaloosa, Alabama 35487, United States; [orcid.org/0000-0002-0215-8210](#)*

**Mohammad Sharifian Gh** — *Department of Cell Biology, University of Virginia, Charlottesville, Virginia 22908, United States*

**Farhad Akbari Afkhami** — *Department of Chemistry and Biochemistry, University of Alabama, Tuscaloosa, Alabama 35487, United States; [orcid.org/0000-0001-5977-8480](#)*

**Mohammad Reza Shirzad Kebria** — *Department of Chemical Engineering, Babol Noshirvani University of Technology, Babol 4714781167, Iran*

**Alberto Tiraferri** — *Department of Environment, Land and Infrastructure Engineering (DIATI), Politecnico di Torino, 10129 Turin, Italy; [orcid.org/0000-0001-9859-1328](#)*

**Marco Sangermano** — *Department of Applied Science and Technology, Politecnico di Torino, 10129 Turin, Italy*

**Milad R. Esfahani** — *Department of Chemical and Biological Engineering, University of Alabama, Tuscaloosa, Alabama 35487, United States; [orcid.org/0000-0001-6530-4310](#)*

Complete contact information is available at: <https://pubs.acs.org/10.1021/acssuschemeng.0c00201>

### Author Contributions

○S.F.S., A.A.S., S.K.S., and M.D.F. contributed equally to this work.

### Notes

The authors declare no competing financial interest.

## REFERENCES

- (1) Marrez, D. A.; Abdelhamid, A. E.; Darwesh, O. M. Eco-Friendly Cellulose Acetate Green Synthesized Silver Nano-Composite as Antibacterial Packaging System for Food Safety. *Food Packag. Shelf Life* **2019**, *20*, 100302.
- (2) Firouzjaei, M. D.; Shamsabadi, A. A.; Sharifian Gh, M.; Rahimpour, A.; Soroush, M. A Novel Nanocomposite with Superior Antibacterial Activity: A Silver-based Metal Organic Framework Embellished with Graphene Oxide. *Adv. Mater. Interfaces* **2018**, *5*, 1701365.
- (3) Firouzjaei, M. D.; Shamsabadi, A. A.; Aktij, S. A.; Seyedpour, S. F.; Sharifian Gh, M.; Rahimpour, A.; Esfahani, M. R.; Ulbricht, M.; Soroush, M. Exploiting Synergetic Effects of Graphene Oxide and a Silver-Based Metal–Organic Framework to Enhance Antifouling and Anti-Biofouling Properties of Thin-Film Nanocomposite Membranes. *ACS Appl. Mater. Interfaces* **2018**, *10*, 42967–42978.
- (4) Abdelhameed, R. M.; El-Sayed, H. A.; El-Shahat, M.; El-Sayed, A. A.; Darwesh, O. M. Novel Triazolothiadiazole and Triazolothiadiazine Derivatives Containing Pyridine Moiety: Design, Synthesis, Bactericidal and Fungicidal Activities. *Curr. Bioact. Compd.* **2018**, *14*, 169–179.
- (5) Firouzjaei, M. D.; Seyedpour, S. F.; Aktij, S. A.; Giagnorio, M.; Bazrafshan, N.; Mollahosseini, A.; Samadi, F.; Ahmadalipour, S.; Firouzjaei, F. D.; Esfahani, M. R.; Tiraferri, A.; Elliott, M.; Sangermano, M.; Abdelrasoul, A.; McCutcheon, J. R.; Sadrzadeh, M.; Esfahani, A. R.; Rahimpour, A. Recent Advances in Functionalized Polymer Membranes for Biofouling Control and Mitigation in Forward Osmosis. *J. Membr. Sci.* **2020**, *596*, 117604.
- (6) Shamsabadi, A. A.; Gh, M. S.; Anasori, B.; Soroush, M. Antimicrobial Mode-of-Action of Colloidal Ti3C2TX MXene Nanosheets. *ACS Sustainable Chem. Eng.* **2018**, *6*, 16586–16596.
- (7) Esfahani, M. R.; Koutahzadeh, N.; Esfahani, A. R.; Firouzjaei, M. D.; Anderson, B.; Peck, L. A Novel Gold Nanocomposite Membrane with Enhanced Permeation, Rejection and Self-Cleaning Ability. *J. Membr. Sci.* **2019**, *573*, 309–319.
- (8) Mozafari, M.; Seyedpour, S. F.; Salestan, S. K.; Rahimpour, A.; Shamsabadi, A. A.; Firouzjaei, M. D.; Esfahani, M. R.; Tiraferri, A.; Mohsenian, H.; Sangermano, M.; Soroush, M. Facile Cu-BTC Surface Modification of Thin Chitosan Film Coated Polyethersulfone

Membranes with Improved Antifouling Properties for Sustainable Removal of Manganese. *J. Membr. Sci.* **2019**, *588*, 117200.

(9) Rahimpour, A.; Seyedpour, S. F.; Aghapour Aktij, S.; Dadashi Firouzjaei, M.; Zirehpour, A.; Arabi Shamsabadi, A.; Khoshhal Salestan, S.; Jabbari, M.; Soroush, M. Simultaneous Improvement of Antimicrobial, Antifouling, and Transport Properties of Forward Osmosis Membranes with Immobilized Highly-Compatible Poly-rhodanine Nanoparticles. *Environ. Sci. Technol.* **2018**, *52*, 5246–5258.

(10) Seyedpour, S. F.; Rahimpour, A.; Najafpour, G. Facile In-Situ Assembly of Silver-Based MOFs to Surface Functionalization of TFC Membrane: A Novel Approach toward Long-Lasting Biofouling Mitigation. *J. Membr. Sci.* **2019**, *573*, 257–269.

(11) Fromm, K. M. Silver Coordination Compounds with Antimicrobial Properties. *Appl. Organomet. Chem.* **2013**, *27*, 683–687.

(12) Mourad, R.; Helaly, F.; Darwesh, O.; Sawy, S. E. Antimicrobial and Physicomechanical Natures of Silver Nanoparticles Incorporated into Silicone-Hydrogel Films. *Contact Lens Anterior Eye* **2019**, *42*, 325–333.

(13) Quadros, M. E.; Marr, L. C. Silver Nanoparticles and Total Aerosols Emitted by Nanotechnology-Related Consumer Spray Products. *Environ. Sci. Technol.* **2011**, *45*, 10713–10719.

(14) Kim, J. S.; Kuk, E.; Yu, K. N.; Kim, J.-H.; Park, S. J.; Lee, H. J.; Kim, S. H.; Park, Y. K.; Park, Y. H.; Hwang, C.-Y.; Kim, Y.-K.; Lee, Y.-S.; Jeong, D. H.; Cho, M.-H. Antimicrobial Effects of Silver Nanoparticles. *Nanomed. Nanotechnol. Biol. Med.* **2007**, *3*, 95–101.

(15) Zirehpour, A.; Rahimpour, A.; Arabi Shamsabadi, A.; Sharifan Gh, M.; Soroush, M. Mitigation of Thin-Film Composite Membrane Biofouling via Immobilizing Nano-Sized Biocidal Reservoirs in the Membrane Active Layer. *Environ. Sci. Technol.* **2017**, *51*, 5511.

(16) Zhang, W. Nanoparticle Aggregation: Principles and Modeling. *Nanomaterial*; Springer, 2014; pp 19–43.

(17) Esfahani, M. R.; Aktij, S. A.; Dabaghian, Z.; Firouzjaei, M. D.; Rahimpour, A.; Eke, J.; Escobar, I. C.; Abolhassani, M.; Greenlee, L. F.; Esfahani, A. R.; Sadmani, A.; Koutahzadeh, N. Nanocomposite Membranes for Water Separation and Purification: Fabrication, Modification, and Applications. *Sep. Purif. Technol.* **2019**, *213*, 465–499.

(18) Abdelhameed, R. M.; Darwesh, O. M.; Rocha, J.; Silva, A. M. S. IRMOF-3 Biological Activity Enhancement by Post-synthetic Modification. *Eur. J. Inorg. Chem.* **2019**, *2019*, 1243–1249.

(19) Huang, W.; Zhu, H.-B.; Gou, S.-H. Self-Assembly Directed by Dinuclear Zinc (II) Macroyclic Species. *Coord. Chem. Rev.* **2006**, *250*, 414–423.

(20) Yeh, C.-W.; Chang, W.-J.; Suen, M.-C.; Lee, H.-T.; Tsai, H.-A.; Tsou, C.-H. Roles of the Anion in the Self-Assembly of Silver (I) Complexes Containing 4-Amino-1,2,4-Triazole. *Polyhedron* **2013**, *61*, 151–160.

(21) Zhuang, W.; Yuan, D.; Li, J.-R.; Luo, Z.; Zhou, H.-C.; Bashir, S.; Liu, J. Highly Potent Bactericidal Activity of Porous Metal-organic Frameworks. *Adv. Healthcare Mater.* **2012**, *1*, 225–238.

(22) Firouzjaei, M. D.; Afkhami, F. A.; Esfahani, M. R.; Turner, C. H.; Nejati, S. Experimental and Molecular Dynamics Study on Dye Removal from Water by a Graphene Oxide-Copper-Metal Organic Framework Nanocomposite. *J. Water Process Eng.* **2020**, *34*, 101180.

(23) Lu, X.; Ye, J.; Sun, Y.; Bogale, R. F.; Zhao, L.; Tian, P.; Ning, G. Ligand Effects on the Structural Dimensionality and Antibacterial Activities of Silver-Based Coordination Polymers. *Dalton Trans.* **2014**, *43*, 10104–10113.

(24) Robin, A. Y.; Fromm, K. M. Coordination Polymer Networks with O-and N-Donors: What They Are, Why and How They Are Made. *Coord. Chem. Rev.* **2006**, *250*, 2127–2157.

(25) Aguado, S.; Quirós, J.; Canivet, J.; Farrusseng, D.; Boltes, K.; Rosal, R. Antimicrobial Activity of Cobalt Imidazolate Metal–Organic Frameworks. *Chemosphere* **2014**, *113*, 188–192.

(26) Cho, H.-Y.; Kim, J.; Kim, S.-N.; Ahn, W.-S. High Yield 1-L Scale Synthesis of ZIF-8 via a Sonochemical Route. *Microporous Mesoporous Mater.* **2013**, *169*, 180–184.

(27) Darwesh, O.; Matter, I.; Eida, M.; Moawad, H.; Oh, Y.-K. Influence of Nitrogen Source and Growth Phase on Extracellular Biosynthesis of Silver Nanoparticles Using Cultural Filtrates of *Scenedesmus Obliquus*. *Appl. Sci.* **2019**, *9*, 1465.

(28) Zirehpour, A.; Rahimpour, A.; Khoshhal, S.; Firouzjaei, M. D.; Ghoreyshi, A. A. The Impact of MOF Feasibility to Improve the Desalination Performance and Antifouling Properties of FO Membranes. *RSC Adv.* **2016**, *6*, 70174–70185.

(29) McCann, M.; Curran, R.; Ben-Shoshan, M.; McKee, V.; Tahir, A. A.; Devereux, M.; Kavanagh, K.; Creaven, B. S.; Kellett, A. Silver (I) Complexes of 9-Anthracenecarboxylic Acid and Imidazoles: Synthesis, Structure and Antimicrobial Activity. *Dalton Trans.* **2012**, *41*, 6516–6527.

(30) Kathiravan, M. K.; Salake, A. B.; Chothe, A. S.; Dudhe, P. B.; Watode, R. P.; Mukta, M. S.; Gadhwe, S. The Biology and Chemistry of Antifungal Agents: A Review. *Bioorg. Med. Chem.* **2012**, *20*, 5678–5698.

(31) Bansal, Y.; Silakari, O. The Therapeutic Journey of Benzimidazoles: A Review. *Bioorg. Med. Chem.* **2012**, *20*, 6208–6236.

(32) Andersson Trojer, M.; Movahedi, A.; Blanck, H.; Nydén, M. Imidazole and Triazole Coordination Chemistry for Antifouling Coatings. *J. Chem.* **2013**, *2013*, 1.

(33) Akhtar, W.; Khan, M. F.; Verma, G.; Shaquizzaman, M.; Rizvi, M. A.; Mehdi, S. H.; Akhter, M.; Alam, M. M. Therapeutic Evolution of Benzimidazole Derivatives in the Last Quinquennial Period. *Eur. J. Med. Chem.* **2017**, *126*, 705–753.

(34) Niehues, M.; Erker, G.; Kehr, G.; Schwab, P. F.; Blacque, O.; Berke, H. *Organometallics* **2002**, *21*, 2905.

(35) Díez-González, S.; Nolan, S. P. Stereoelectronic Parameters Associated with N-Heterocyclic Carbene (NHC) Ligands: A Quest for Understanding. *Coord. Chem. Rev.* **2007**, *251*, 874–883.

(36) Cavallo, L.; Correa, A.; Costabile, C.; Jacobsen, H. Steric and Electronic Effects in the Bonding of N-Heterocyclic Ligands to Transition Metals. *J. Organomet. Chem.* **2005**, *690*, 5407–5413.

(37) Samantaray, M. K.; Pang, K.; Shaikh, M. M.; Ghosh, P. From Large 12-Membered Macrometallacycles to Ionic (NHC) 2M<sup>+</sup> Cl<sup>-</sup> Type Complexes of Gold and Silver by Modulation of the N-Substituent of Amido-Functionalized N-Heterocyclic Carbene (NHC) Ligands. *Inorg. Chem.* **2008**, *47*, 4153–4165.

(38) Aragoni, M. C.; Arca, M.; Demartin, F.; Devillanova, F. A.; Garau, A.; Isaia, F.; Lippolis, V.; Verani, G. Anti-Thyroid Drug Methimazole: X-Ray Characterization of Two Novel Ionic Disulfides Obtained from Its Chemical Oxidation by I<sub>2</sub>. *J. Am. Chem. Soc.* **2002**, *124*, 4538.

(39) Meyer, S.; Demeshko, S.; Dechert, S.; Meyer, F. Synthesis, Structure and Mossbauer Characterization of Polymeric Iron(II) Complexes with Bidentate Thiourea Ligands. *Inorg. Chim. Acta* **2010**, *363*, 3088.

(40) Jia, W.-G.; Huang, Y.-B.; Lin, Y.-J.; Wang, G.-L.; Jin, G.-X. Nickel Complexes and Cobalt Coordination Polymers with Organochalcogen (S, Se) Ligands Bearing an N-Methylimidazole Moiety: Syntheses, Structures, and Properties. *Eur. J. Inorg. Chem.* **2008**, *2008*, 4063–4073.

(41) Jia, W.-G.; Huang, Y.-B.; Lin, Y.-J.; Jin, G.-X. Syntheses and Structures of Half-Sandwich Iridium(III) and Rhodium(III) Complexes with Organochalcogen (S, Se) Ligands Bearing N-Methylimidazole and Their Use as Catalysts for Norbornene Polymerization. *Dalton Trans.* **2008**, *5612–5620*.

(42) Zhang, Y.; Jia, Y.; Hou, L. a. Synthesis of Zeolitic Imidazolate Framework-8 on Polyester Fiber for PM 2.5 Removal. *RSC Adv.* **2018**, *8*, 31471–31477.

(43) Zhang, L.; Wang, J.; Ren, X.; Zhang, W.; Zhang, T.; Liu, X.; Du, T.; Li, T.; Wang, J. Internally Extended Growth of Core–Shell NH 2-MIL-101 (Al)<sub>n</sub> ZIF-8 Nanoflowers for the Simultaneous Detection and Removal of Cu (II). *J. Mater. Chem. A* **2018**, *6*, 21029–21038.

(44) Mahmoodi, N. M.; Oveisi, M.; Bakhtiari, M.; Hayati, B.; Shekarchi, A. A.; Bagheri, A.; Rahimi, S. Environmentally Friendly Ultrasound-Assisted Synthesis of Magnetic Zeolitic Imidazolate Framework-Graphene Oxide Nanocomposites and Pollutant Removal from Water. *J. Mol. Liq.* **2019**, *282*, 115–130.

(45) Huang, D.; Xin, Q.; Ni, Y.; Shuai, Y.; Wang, S.; Li, Y.; Ye, H.; Lin, L.; Ding, X.; Zhang, Y. Synergistic Effects of Zeolite Imidazole Framework@ Graphene Oxide Composites in Humidified Mixed Matrix Membranes on CO<sub>2</sub> Separation. *RSC Adv.* **2018**, *8*, 6099–6109.

(46) Sarango, L.; Benito, J.; Gascón, I.; Zornoza, B.; Coronas, J. Homogeneous Thin Coatings of Zeolitic Imidazolate Frameworks Prepared on Quartz Crystal Sensors for CO<sub>2</sub> Adsorption. *Microporous Mesoporous Mater.* **2018**, *272*, 44–52.

(47) He, M.; Yao, J.; Liu, Q.; Wang, K.; Chen, F.; Wang, H. Facile Synthesis of Zeolitic Imidazolate Framework-8 from a Concentrated Aqueous Solution. *Microporous Mesoporous Mater.* **2014**, *184*, 55–60.

(48) Xu, F.; Kou, L.; Jia, J.; Hou, X.; Long, Z.; Wang, S. Metal–Organic Frameworks of Zeolitic Imidazolate Framework-7 and Zeolitic Imidazolate Framework-60 for Fast Mercury and Methyl-mercury Speciation Analysis. *Anal. Chim. Acta* **2013**, *804*, 240–245.

(49) Tu, M.; Wiktor, C.; Rösler, C.; Fischer, R. A. Rapid Room Temperature Syntheses of Zeolitic-Imidazolate Framework (ZIF) Nanocrystals. *Chem. Commun.* **2014**, *50*, 13258–13260.

(50) Trivedi, M. K.; Branton, A.; Trivedi, D.; Nayak, G. Physical and Structural Characterization of Biofield Treated Imidazole Derivatives. *Nat. Prod. Chem. Res.* **2015**, *3*, 5.

(51) Visser, J. W. A Fully Automatic Program for Finding the Unit Cell from Powder Data. *J. Appl. Crystallogr.* **1969**, *2*, 89–95.

(52) Boultif, A.; Louër, D. Indexing of Powder Diffraction Patterns for Low-Symmetry Lattices by the Successive Dichotomy Method. *J. Appl. Crystallogr.* **1991**, *24*, 987–993.

(53) Huang, X.-C.; Li, D.; Chen, X.-M. Solvent-Induced Supramolecular Isomerism in Silver(i) 2-Methylimidazolate. *CrystEngComm* **2006**, *8*, 351–355.

(54) Novak, S.; Maver, U.; Peternel, Š.; Venturini, P.; Bele, M.; Gaberšček, M. Electrophoretic Deposition as a Tool for Separation of Protein Inclusion Bodies from Host Bacteria in Suspension. *Colloids Surf, A* **2009**, *340*, 155–160.

(55) Schwegmann, H.; Feitz, A. J.; Frimmel, F. H. Influence of the Zeta Potential on the Sorption and Toxicity of Iron Oxide Nanoparticles on *S. Cerevisiae* and *E. Coli*. *J. Colloid Interface Sci.* **2010**, *347*, 43–48.

(56) Ma, W.; Soroush, A.; Luong, T. V. A.; Rahaman, M. S. Cysteamine- and Graphene Oxide-Mediated Copper Nanoparticle Decoration on Reverse Osmosis Membrane for Enhanced Anti-Microbial Performance. *J. Colloid Interface Sci.* **2017**, *501*, 330.

(57) Park, S.-H.; Kim, S. H.; Park, S.-J.; Ryoo, S.; Woo, K.; Lee, J. S.; Kim, T.-S.; Park, H.-D.; Park, H.; Park, Y.-I.; et al. Direct Incorporation of Silver Nanoparticles onto Thin-Film Composite Membranes via Arc Plasma Deposition for Enhanced Antibacterial and Permeation Performance. *J. Membr. Sci.* **2016**, *513*, 226.

(58) Tang, C.; Kwon, Y.; Leckie, J. Probing the Nano- and Micro-Scales of Reverse Osmosis Membranes-A Comprehensive Characterization of Physiochemical Properties of Uncoated and Coated Membranes by XPS, TEM, ATR-FTIR, and Streaming Potential Measurements. *J. Membr. Sci.* **2007**, *287*, 146.

(59) Ang, H.; Hong, L. Polycationic Polymer-Regulated Assembling of 2D MOF Nanosheets for High-Performance Nanofiltration. *ACS Appl. Mater. Interfaces* **2017**, *9*, 28079–28088.

(60) Kundu, S.; Malik, B.; Pattanayak, D. K.; Pillai, V. K. Effect of Dimensionality and Doping in Quasi-“One-Dimensional (1-D)” Nitrogen-Doped Graphene Nanoribbons on the Oxygen Reduction Reaction. *ACS Appl. Mater. Interfaces* **2017**, *9*, 38409–38418.

(61) Jian, M.; Liu, B.; Zhang, G.; Liu, R.; Zhang, X. Adsorptive Removal of Arsenic from Aqueous Solution by Zeolitic Imidazolate Framework-8 (ZIF-8) Nanoparticles. *Colloids Surf, A* **2015**, *465*, 67–76.

(62) Li, Y.; Cai, X.; Chen, S.; Zhang, H.; Zhang, K. H. L.; Hong, J.; Chen, B.; Kuo, D.-H.; Wang, W. Highly Dispersed Metal Carbide on ZIF-Derived Pyridinic-N-Doped Carbon for CO<sub>2</sub> Enrichment and Selective Hydrogenation. *ChemSusChem* **2018**, *11*, 1040–1047.

(63) Deng, Y.; Dong, Y.; Wang, G.; Sun, K.; Shi, X.; Zheng, L.; Li, X.; Liao, S. Well-Defined ZIF-Derived Fe–N Codoped Carbon Nanoframes as Efficient Oxygen Reduction Catalysts. *ACS Appl. Mater. Interfaces* **2017**, *9*, 9699–9709.

(64) Jin, L.-N.; Liu, Q.; Sun, W.-Y. An Introduction to Synthesis and Application of Nanoscale Metal–Carboxylate Coordination Polymers. *CrystEngComm* **2014**, *16*, 3816–3828.

(65) Jung, S.; Cho, W.; Lee, H. J.; Oh, M. Self-template-directed Formation of Coordination-polymer Hexagonal Tubes and Rings, and Their Calcination to ZnO Rings. *Angew. Chem., Int. Ed.* **2009**, *48*, 1459–1462.

(66) Masoomi, M. Y.; Morsali, A. Applications of Metal–Organic Coordination Polymers as Precursors for Preparation of Nano-Materials. *Coord. Chem. Rev.* **2012**, *256*, 2921–2943.

(67) Krokidas, P.; Moncho, S.; Brothers, E. N.; Castier, M.; Economou, I. G. Tailoring the Gas Separation Efficiency of Metal Organic Framework ZIF-8 through Metal Substitution: A Computational Study. *Phys. Chem. Chem. Phys.* **2018**, *20*, 4879–4892.

(68) Bhattacharyya, S.; Das, C.; Maji, T. K. MOF Derived Carbon Based Nanocomposite Materials as Efficient Electrocatalysts for Oxygen Reduction and Oxygen and Hydrogen Evolution Reactions. *RSC Adv.* **2018**, *8*, 26728–26754.

(69) Hughes, J. T.; Sava, D. F.; Nenoff, T. M.; Navrotsky, A. Thermochemical Evidence for Strong Iodine Chemisorption by ZIF-8. *J. Am. Chem. Soc.* **2013**, *135*, 16256–16259.

(70) Srivastava, M.; Roy, P. K.; Ramanan, A. Hydrolytically Stable ZIF-8@PDMS Core–Shell Microspheres for Gas–Solid Chromatographic Separation. *RSC Adv.* **2016**, *6*, 13426–13432.

(71) McCann, M.; Curran, R.; Ben-Shoshan, M.; McKee, V.; Devereux, M.; Kavanagh, K.; Kellett, A. Synthesis, Structure and Biological Activity of Silver(I) Complexes of Substituted Imidazoles. *Polyhedron* **2013**, *56*, 180–188.

(72) Adarsh, N. N.; Novio, F.; Ruiz-Molina, D. Coordination Polymers Built from 1,4-Bis(Imidazole-1-Ylmethyl)Benzene: From Crystalline to Amorphous. *Dalton Trans.* **2016**, *45*, 11233–11255.

(73) Behera, N.; Manivannan, V. Molecular Structures of Some Bivalent Metal Complexes of 1-(4-Acetylphenyl)Imidazole and Co-Ligands. *Polyhedron* **2018**, *149*, 84–94.

(74) Cheng, D.; Khan, M. A.; Houser, R. P. Coordination Polymers Composed of Copper(II), Trimesic Acid, and Imidazole: 3D Architecture Stabilized by Hydrogen Bonding. *Inorg. Chem.* **2001**, *40*, 6858–6859.

(75) Liu, K.; Sun, Y.; Deng, L.; Cao, F.; Han, J.; Wang, L. Cu(II) Coordination Polymers Constructed by Tetrafluoroterephthalic Acid and Varied Imidazole-Containing Ligands: Syntheses, Structures and Properties. *J. Solid State Chem.* **2018**, *258*, 24–31.

(76) Schieber, N. P.; Combs, S.; Vakiti, R. K.; Yan, B.; Webb, C. Hydrogen-Bonded Sodium–Organic Frameworks from Imidazole-4, 5-Dicarboxylic Acid. *J. Coord. Chem.* **2012**, *65*, 4177–4184.

(77) Yaman, P. K.; Erer, H. Novel Coordination Compounds Based on 2-Methylimidazole and 2,2'-Dimethylglutarate Containing Ligands: Synthesis and Characterization. *J. Turk. Chem. Soc., Sect. A* **2018**, *5*, 953–962.

(78) Jin, T.; Zhou, J.; Pan, Y.; Huang, Y.; Jin, C. Self-Assembled 1D Infinite Inorganic [2]Catenane and 2D Sheet Framework with Calix[8]Phenylazimidazole and [4+4]Metallomacrocyclic Motifs Based on Silver and Ditopic Bis(Imidazolyl)Methane Ligands. *J. Mol. Struct.* **2018**, *1160*, 222–226.

(79) Grossman, L. I.; Watson, R.; Vinograd, J. Restricted Uptake of Ethidium Bromide and Propidium Diiodide by Denatured Closed Circular DNA in Buoyant Cesium Chloride. *J. Mol. Biol.* **1974**, *86*, 271.

(80) Yeh, C.-J. G.; Hsi, B.-L.; Page Faulk, W. Propidium Iodide as a Nuclear Marker in Immunofluorescence. II. Use with Cellular Identification and Viability Studies. *J. Immunol. Methods* **1981**, *43*, 269.

(81) Hudson, B.; Upholt, W. B.; Devinny, J.; Vinograd, J. The Use of an Ethidium Analogue in the Dye-Buoyant Density Procedure for the Isolation of Closed Circular DNA: The Variation of the Superhelix Density of Mitochondrial DNA. *Proc. Natl. Acad. Sci. U.S.A.* **1969**, *62*, 813.

(82) Tas, J.; Westerneng, G. Fundamental Aspects of the Interaction of Propidium Diiodide with Nuclei Acids Studied in a Model System of Polyacrylamide Films. *J. Histochem. Cytochem.* **1981**, *29*, 929.

(83) Singh, M. P. Rapid Test for Distinguishing Membrane-Active Antibacterial Agents. *J. Microbiol. Methods* **2006**, *67*, 125–130.

(84) Alimohammadi, F.; Sharifian Gh, M.; Attanayake, N. H.; Thenuwara, A. C.; Gogotsi, Y.; Anasori, B.; Strongin, D. R. Antimicrobial Properties of 2D  $\text{MnO}_2$  and  $\text{MoS}_2$  Nanomaterials Vertically Aligned on Graphene Materials and  $\text{Ti}_3\text{C}_2$  MXene. *Langmuir* **2018**, *34*, 7192–7200.

(85) Hindi, K. M.; Siciliano, T. J.; Durmus, S.; Panzner, M. J.; Medvetz, D. A.; Reddy, D. V.; Hogue, L. A.; Hovis, C. E.; Hilliard, J. K.; Mallet, R. J.; et al. Synthesis, Stability, and Antimicrobial Studies of Electronically Tuned Silver Acetate N-Heterocyclic Carbenes. *J. Med. Chem.* **2008**, *51*, 1577–1583.

(86) Berchel, M.; Gall, T. L.; Denis, C.; Hir, S. L.; Quentel, F.; Elléouet, C.; Montier, T.; Rueff, J.-M.; Salaün, J.-Y.; Haelters, J.-P.; et al. A Silver-Based Metal-Organic Framework Material as a “Reservoir” of Bactericidal Metal Ions. *New J. Chem.* **2011**, *35*, 1000.

(87) Slenters, T. V.; Hauser-Gerspach, I.; Daniels, A. U.; Fromm, K. M. Silver Coordination Compounds as Light-Stable, Nano-Structured and Anti-Bacterial Coatings for Dental Implant and Restorative Materials. *J. Mater. Chem.* **2008**, *18*, 5359.

(88) Gordon, O.; Vig Slenters, T.; Brunetto, P. S.; Villaruz, A. E.; Sturdevant, D. E.; Otto, M.; Landmann, R.; Fromm, K. M. Silver Coordination Polymers for Prevention of Implant Infection: Thiol Interaction, Impact on Respiratory Chain Enzymes, and Hydroxyl Radical Induction. *Antimicrob. Agents Chemother.* **2010**, *54*, 4208–4218.

(89) Kumar, R.; Münstedt, H. Silver Ion Release from Antimicrobial Polyamide/Silver Composites. *Biomaterials* **2005**, *26*, 2081–2088.

(90) Lu, X.; Ye, J.; Zhang, D.; Xie, R.; Bogale, R. F.; Sun, Y.; Zhao, L.; Zhao, Q.; Ning, G. Silver Carboxylate Metal-Organic Frameworks with Highly Antibacterial Activity and Biocompatibility. *J. Inorg. Biochem.* **2014**, *138*, 114.

(91) Rueff, J.-M.; Perez, O.; Caignaert, V.; Hix, G.; Berchel, M.; Quentel, F.; Jaffrès, P.-A. Silver-Based Hybrid Materials from Meta- or Para-Phosphonobenzoic Acid: Influence of the Topology on Silver Release in Water. *Inorg. Chem.* **2015**, *54*, 2152–2159.

(92) Chernousova, S.; Epple, M. Silver as Antibacterial Agent: Ion, Nanoparticle, and Metal. *Angew. Chem., Int. Ed.* **2013**, *52*, 1636.

(93) Zhao, X.; Zhang, R.; Liu, Y.; He, M.; Su, Y.; Gao, C.; Jiang, Z. Antifouling Membrane Surface Construction: Chemistry Plays a Critical Role. *J. Membr. Sci.* **2018**, *551*, 145–171.

(94) Yuan, X.; Setyawati, M. I.; Tan, A. S.; Ong, C. N.; Leong, D. T.; Xie, J. Highly Luminescent Silver Nanoclusters with Tunable Emissions: Cyclic Reduction–Decomposition Synthesis and Antimicrobial Properties. *NPG Asia Mater.* **2013**, *5*, No. e39.

(95) Xiu, Z.-m.; Zhang, Q.-b.; Puppala, H. L.; Colvin, V. L.; Alvarez, P. J. J. Negligible Particle-Specific Antibacterial Activity of Silver Nanoparticles. *Nano Lett.* **2012**, *12*, 4271.

(96) Tamames-Tabar, C.; Imbuluzqueta, E.; Guillou, N.; Serre, C.; Miller, S. R.; Elkaïm, E.; Horcajada, P.; Blanco-Prieto, M. J. A Zn Azelate MOF: Combining Antibacterial Effect. *CrystEngComm* **2015**, *17*, 456–462.

(97) Pal, S.; Tak, Y. K.; Song, J. M. Does the Antibacterial Activity of Silver Nanoparticles Depend on the Shape of the Nanoparticle? A Study of the Gram-Negative Bacterium *Escherichia Coli*. *Appl. Environ. Microbiol.* **2007**, *73*, 1712–1720.

(98) Gondikas, A. P.; Morris, A.; Reinsch, B. C.; Marinakos, S. M.; Lowry, G. V.; Hsu-Kim, H. Cysteine-Induced Modifications of Zero-Valent Silver Nanomaterials: Implications for Particle Surface Chemistry, Aggregation, Dissolution, and Silver Speciation. *Environ. Sci. Technol.* **2012**, *46*, 7037–7045.